International Journal of Mechanical, Industrial and Aerospace Sciences
ISSN: 2517-9950
Vol:1, No:8, 2007

A Large-Eddy Simulation of Vortex Cell flow with Incoming Turbulent Boundary Layer

Arpiruk Hokpunna, and Michael Manhart

***Abstract*—**We present a Large-Eddy simulation of a vortex cell with circular shaped. The results show that the flow field can be sub divided into four important zones, the shear layer above the cavity, the stagnation zone, the vortex core in the cavity and the boundary layer along the wall of the cavity. It is shown that the vortex core consits of solid body rotation without much turbulence activity. The vortex is mainly driven by high energy packets that are driven into the cavity from the stagnation point region and by entrainment of fluid from the cavity into the shear layer. The physics in the boundary layer along the cavity's wall seems to be far from that of a canonical boundary layer which might be a crucial point for modelling this flow.

***Keywords*—**Turbulent flow, Large eddy simulations, boundary layer and cavity flow, vortex cell flow.

I. Introduction

LIFT enhancement and drag reduction is one of the most demanding technology in aviation industry. To ensure a high lift-to-drag ratio, wings of modern aircraft are thin and streamlined. However, from a structural-strength viewpoint, in order to carry a larger load having thick wing would be beneficial. As the progress in aviation leads to an increase in the size of transport aircraft, the balance between structural-strength and aerodynamics quality shifts in favour of a thick wing. The flow past a thick airfoil, however, is likely to separate, which affects the aerodynamic performance of the wing. The problem, therefore, is to resolve the contradiction between aerodynamic and structural requirements on the wing design. The project "VortexCell2050" is a research project aims at solving this problem by combining two advanced technologies: trapped vortex and active control.

Trapping vortices is a technology for preventing vortex shedding and reducing drag in flows past bluff bodies. Large vortices forming in high-speed flows past bluff bodies tend to be shed downstream, with new vortices forming in their stead (Fig.1). This results in increased drag, unsteady loads on the body, and produces an unsteady wake. If the vortex is kept near the body at all times it is called trapped. Vortices can be trapped in vortex cells, as in Fig.2.

Control algorithms must be robust and fast, thus solving three-dimensional problems are not allowed. An insightful understanding of the physics in vortex cell flows is required to create a two-dimensional turbulence model that is sufficiently accurate and affordable in real-time control. In order achieve this aim, Large-Eddy simulations (LES) is an only a viable option that can represent the highly transient and three dimensional nature of the problem at sufficient accuracy within affordable time. As a part of the investigation of vortex cell flows, we study a vortex cell flow with homogeneous spanwise direction. This will serve as the two-dimensional limit where LES and numerical simulation of Reynolds-Averaged Navier-Stokes equations(RANS) should agree. In a later phase of the study, effects of finite spanwise and direction of incoming flow can be identified using this simulation as a based comparison. This paper aims to present the investigation of the flow physics inside the vortex cell with circular shape by means of large-eddy simulation. We investigate first and second order statistics of the flow field in profiles and 2D distributions.

Arpiruk Hokpunna is with the Fachgebiet Hydromechanik, Technische Universitaet Muenchen, Munich, Germany email: a.hokpunna@bv.tum.de.
Michael Manhart, email: m.manhart@bv.tum.de.

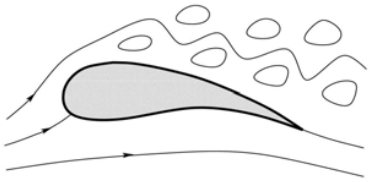

Fig. 1 Continuously shedding vortices

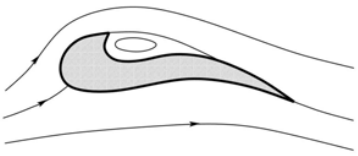

Fig. 2 Trapped vortex cell

II. Numerical Approaches

We solve the Navier-Stokes equations for incompressible Newtonian flows:

$$\frac{\partial u_i}{\partial x_i} = 0 \tag{1}$$

$$\frac{\partial u_i}{\partial t} + \frac{\partial u_i u_j}{\partial x_j} = -\frac{1}{\rho}\frac{\partial p}{\partial x_i} + \nu \frac{\partial^2 u_i}{\partial x_j^2} \tag{2}$$

The Navier-Stokes equations (NSE) are integrated within the standard framework of Finite Volumes using staggered Cartesian grids [5]. The spatial approximations are second order accurate and use centered interpolations and differentiations. Time integration is performed via a fractional step method using a third-order Runge-Kutta scheme. The pressure

is obtained by a projection formulation at the end of each substep. The Poisson equation is solved by Stone's strongly implicit procedure (SIP). See e.g. Ferziger and Peric [6] for a review on these standard methods.

A. Large-Eddy Simulation and Subgrid-Scale Model

When using Direct Numerical Simulations (DNS) there is no doubt in the accuracy, if the grid is sufficiently resolved. However, the computational cost of DNS is hardly feasible for complex flows at high Reynolds number such as the vortex cell flow we intend to study. Therefore LES is the only possibility to investigate this type of flow.

LES is based on the assumption that the quantities describing the turbulent flow can be decomposed into large scales and small scales. The large scales contain most of the energy and most of the flow information. However, the large scales interact with the small scales and evolve in time. Therefore the small scales cannot be neglected even if we are only interested in the large scales. The goal of LES is to accurately compute the large flow structures and model the effect of the small scales together with their interaction with the large scale structure.

The large scale structures are determined by a spatial filtering operations. The effect caused by the small scale structures are modeled by the subgrid scale tensor (SGS). The filtered NSE are defined as :

$$\frac{\partial \overline{u}_i}{\partial x_i} = 0 \tag{3}$$

$$\frac{\partial \overline{u}_i}{\partial t} + \frac{\partial \overline{u_i u_j}}{\partial x_j} = -\frac{1}{\rho}\frac{\partial \overline{p}}{\partial x_i} + \nu \frac{\partial^2 \overline{u}_i}{\partial x_j^2} \tag{4}$$

When the filtered NSE are solved numerically, only the filtered quantities are available. Therefore the nonlinear convective term $\overline{u_i u_j}$ is approximated by

$$\overline{u_i u_j} = \overline{u}_i \overline{u}_j + \tau_{ij}, \tag{5}$$

where τ_{ij} represents the subgrid scale stress (SGS) tensor. Hence the filtered momentum equation becomes.

$$\frac{\partial \overline{u}_i}{\partial t} + \frac{\partial \overline{u}_i \overline{u}_j}{\partial x_j} = -\frac{1}{\rho}\frac{\partial \overline{p}}{\partial x_i} + \nu \frac{\partial^2 \overline{u}_i}{\partial x_j^2} - \frac{\partial \tau_{ij}}{\partial x_j} \tag{6}$$

There are several possibilities to approximate the SGS tensor τ_{ij}. The most widely known model is the Smagorinsky model [1] which associates the subgrid stress tensor with an eddy viscosity.

$$\tau_{ij} = -2\nu_t \overline{S}_{ij} \tag{7}$$

$$\nu_t = {C_s}^2 \Delta^2 |\overline{S}| \tag{8}$$

Where $\overline{S}_{ij}$ is the rate of strain tensor and Δ is the filter width:

$$\overline{S}_{ij} = \frac{1}{2}\left(\frac{\partial \overline{u}_i}{\partial x_j} + \frac{\partial \overline{u}_j}{\partial x_i}\right) \tag{9}$$

In this simulation we use a Lagrangian SGS model [3] which proposes to compute the average of the Germano identity and minimise the error over the fluid particle trajectories rather than the homogeneous direction.

B. Numerical Boundary Conditions

At solid boundaries, we apply Dirichlet boundary conditions for the velocity and Neumann boundary conditions for the pressure. The complex shaped body is handled by an Immersed boundary technique [4].

The time-dependent turbulent inflow condition is constructed by a superposition of fluctuations onto a time-averaged velocity profile. The time averaged profile is taken from DNS calculations of Spalart [7], the fluctuations are extracted at $x/\delta_0 = 10$ downstream of the inlet by computing the difference between the instantaneous velocity and the one which was averaged in spanwise direction. This method has proven to be useful in previous direct numerical simulations of turbulent boundary layers [8] and shown to be equivalent to the one proposed by Lund [9]

The top of the computational domain is assumed to be a slip surface. The bottom boundary condition is given by the no-slip walls of the cavity. The zero-gradient is imposed at outflow boundary together with strong grid stretching ratio.

C. Immersed Boundary Method

The basic concept of our immersed boundary method is a functional fitting. A certain approximated function $f(x, y, z)$ is assumed to represent the velocity field and boundary condition locally near the interpolating point. This function is determined by method of undetermined coefficients. Once the approximated function is obtained, velocity components at a given point can be obtained. Lagrange polynomial, cubic spline and least square polynomial are available in our code. Detail information about the immersed boundary method can be found in [4].

III. Configuration of Computational Domain

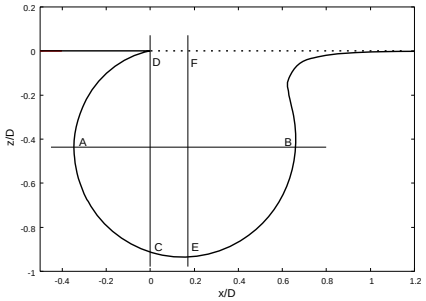

Fig. 3 Cavity cell

The shape of the cavity are shown in figure 3. The reference length is the cavity diameter, D. Flatplate is attached to both ends of the cavity surface shown in 3. The computational box is $[Lx, Ly, Lz] = [6D, 2D, 5D]$ in streamwise, spanwise and wall normal direction, respectively. The origin of the coordinate system is located at the cavity leading edge (cusp). The turbulent inflow boundary condition is set at $x = -2.85D$, its generation will be documented in the next subsection. A zero-gradient velocity and zero (total) pressure is imposed at the outflow plane to which the grid is highly compressed to

reduce wiggles. A slip condition is imposed at the top wall at $z = 4D$. All the solid surfaces are treated by the Immersed Boundary method. A block structured Cartesian grid is used to represent the flow domain. This consists of a sub domain covering the channel above the cavity and one covering the cavity only.

The total number of grid cells is $[Nx, Ny, Nz] = [304, 50, 110]$ in the channel and $[Nx, Ny, Nz] = [166, 50, 80]$ in the cavity grid which add up to $2.34 \cdot 10^6$ grid cells. At their interface, both grids match in all three directions. In streamwise direction, cells are clustered at the rounded impingement edge $\Delta x = 0.003968D$ and towards the outflow plane $\Delta x = 0.03292D$. In spanwise direction, an equidistant grid with $\Delta y = 0.04D$ is used. In wall normal direction, a strong clustering at $z = 0$ for the wall and shear layer resolution is used with $\Delta z_{min} = 0.0025D$.

IV. Results

In this section, we present profiles of time and spatially averaged velocity profiles at locations of interest as indicated in figure 3. The averaging has been done over a time span of $40D/u_\infty$ and in spanwise direction. Our focus here lies on the description of the vortex inside the cavity, the boundary layer along the cavity's wall and the shear layer bounding the cavity. If available, we compare our results with profiles provided by Dr. Iannelli (CIRA).

A. Time-Averaged Quantities – Profiles

The mean velocity profiles inside the cavity in figure IV-A and IV-A are shown along with the RANS simulation provided by Dr.Iannelli of CIRA. These profiles represent the flow across the lines $\overline{EF}$ and $\overline{AB}$. In the centre of the cavity, the profiles are nearly straight lines which indicates solid body rotation in this region. The differences between LES and RANS can be summarised as follows. LES predicts a higher velocity in the shear layer above the cavity and a fuller boundary layer profile. The inner part of the vortex rotates slightly faster in the LES. But, the RANS gives higher peak velocities that are closer at the cavity wall than the peaks of the LES. The peak velocity and its distance could be taken to characterise the boundary layer that is formed by the vortex at the cavity's wall. As the peaks slow down, they move away from the wall during travelling from point B to A. The spanwise vorticity at line $\overline{AB}$, assumes a plateau in the vortex core (Figure IV-A).

In what follows, we consider the Reynolds normal and shear stresses on the same lines as the mean velocities. Note, that at line $\overline{AB}$, the w_{rms} is in streamwise direction of the local flow direction. We check if these R.M.S. values could fit to the boundary layer along the cavity's wall. From figure IV-A we learn that at point B the local free stream velocity is approx $u_l = 0.25u_\infty$. Based on this velocity, the R.M.S. (figure 7) assume approximately $0.28u_l$, $0.24u_l$ and $0.18u_l$, in local streamwise, spanwise and normal direction, which is much larger than what can be observed in canonical boundary layers. In addition, the local boundary layer thickness is smaller than $0.05D$. However, the thicknesses of the R.M.S. at point B are approximately three times larger. At point E, we observe that the turbulent kinetic energy is equally distributed among all three components at a level of approximately $0.24u_l$ and still extending far more away from the wall than the local boundary layer thickness. At point A, the high turbulence levels have undergone a decay but still are way too strong to stem from a canonical boundary layer. The behaviour of the Reynolds normal stresses is far from that of a canonical zero pressure gradient boundary layer along the cavity wall – with all consequences for modelling.

The Reynolds shear stress $< u'w' >$ is plotted along lines $\overline{AB}$ and $\overline{EF}$ in figure 8 and 9. The shear stress behaves in a complicated way. First, it can be stated that is is antisymmetric on line $\overline{AB}$ with respect to the centre of the cavity with three relative extrema. At point B, we observe two local extrema that could correspond to the shear stress produced within the boundary layer along the cavity's wall. This suggest existence of back flow under the shoulder cavity, because it has the right sign and approximately the right position within the boundary layer thickness. When moving further to point E, the peak near the cavity's wall still having the same strength while the second peak is almost disappeared. The near wall peak has the right sign to be able to stem from production within the boundary layer and has also the right thickness. From this development one could argue that the boundary layer along the cavity produces a reasonable shear stress. If that was true and would continue downstream of the boundary layer along the cavity's wall, then at point A, we would expect a negative $< u'w' >$, since the main production term in the balance equation for $u'w'$ is negative $P_{13} = - < u'w' > \partial W/\partial x < 0$. The result shown in figure 9 confirm this expectation.

In what follows, we concentrate on the development of the shear layer bounding the cavity along line $\overline{DG}$. This shear layer drives the vortex inside the cavity by exchanging momentum by viscous and – more importantly – turbulent stresses. In figure 8 we plotted already the turbulent shear stress $< u'w' >$ on two streamwise positions within the shear layer. Directly at the cusp above the cavity ($z > 0$), there is the shear stress profile coming from the boundary layer upstream which has negative sign and a thin positive peak of $< u'w' >$ just beneath the cusp coming from the cavity. At $0.2D$ downstream, the thin shear layer has produced a second peak with negative $< u'w' >$ which is much stronger than the two peaks that are observable at the separation from the cusp. The instabilities within the shear layer seem to be excited very fast which is certainly the result of the returning turbulence convected by the vortex inside the cavity. The streamwise development of the wall normal velocity component and the Reynolds normal stresses is plotted in figure 10. Just after the cusp, the normal component is positive as a consequence of the finite angle of the cusp. As the shear layer widens, the normal velocity turns its sign and transports fluid towards the cavity. As the impingement edge is approached it changes sign again which seems to be the result of the fluid moving away from the stagnation point. The normal Reynolds stresses undergo a fast transition towards a plateau that lasts until the region over the impingement edge is reached. The velocity difference could be estimated as large as approximately $u_s = 0.6u_\infty$. With that

in mind, one would expect from plane mixing layer results values in the range of $0.1u_\infty$ and $0.08u_\infty$ for the streamwise and both, vertical and spanwise components, respectively. It is surprising that the vertical component stays within these expectations, but the other two components are higher by about 50%.

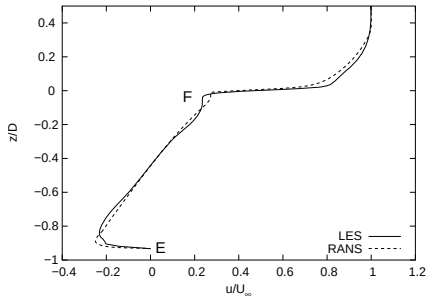

Fig. 4. $< u >$ along $\overline{EF}$.

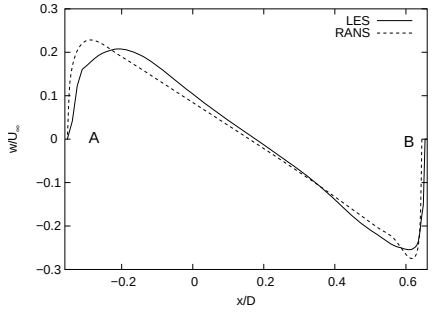

Fig. 5. $< w >$ along $\overline{AB}$.

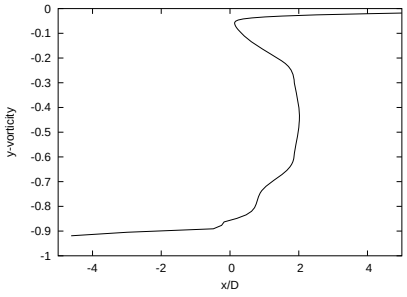

Fig. 6. ω_y at $x = 0.0$.

B. Time Averaged Quantities –Spatial Distribution

In this section, we consider the spatial distribution of the time (and spatial) averaged quantities, i.e. first and second statistical moments. As the flow is homogeneous in spanwise direction, it is sufficient to consider two-dimensional plots in a streamwise-vertical plane. As mentioned already in the previous section, the dominant feature of the flow consists of the vortex inside the cavity that is driven by the shear layer which creates a strong exchange of fluid between the the trapped vortex and the shear layer. The flow field can be divided into several important zones:

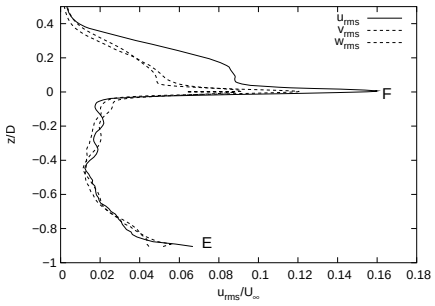

(a)

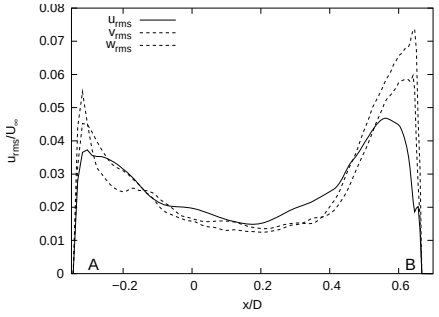

(b)

Fig. 7. R.M.S. of velocity fluctuations normalised by free stream velocity. (a) along $\overline{EF}$. (b) along $\overline{AB}$.

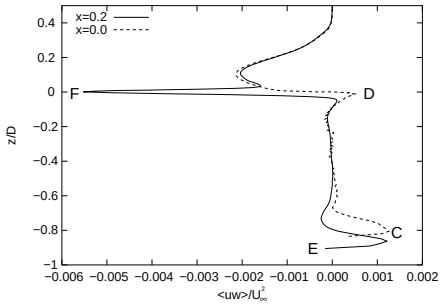

Fig. 8. Reynolds shear stress normalised by free stream velocity along $\overline{EF}$

- *Shear layer*: The shear layer that is forming between outer boundary layer flow and inner cavity flow.
- *Stagnation point*: It is the point of flow reversal and low kinetic energy above the shoulder of the impingement edge of the cavity.
- *Vortex core*: The region with low energy at the core of the cavity which is characterised by dominantly circular motion (solid body rotation).

The *shear layer* between outer and cavity flow is seen in the strong change in u component and kinetic energy of the mean flow field (figure 11). From the latter, the spreading of the shear layer is identified best. It doesn't start immediately downstream of the separation point at the cavity's cusp, although we have seen in the previous section that the turbulent stresses undergo a jump immediately after the cusp. This might be due to the fact that the flow coming from inside the cavity

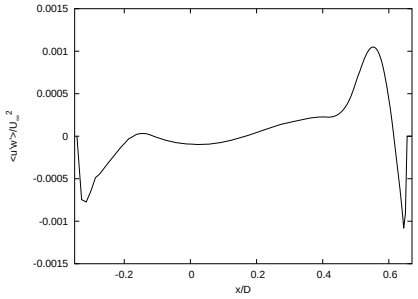

Fig. 9. Reynolds shear stress normalised by free stream velocity along $\overline{AB}$.

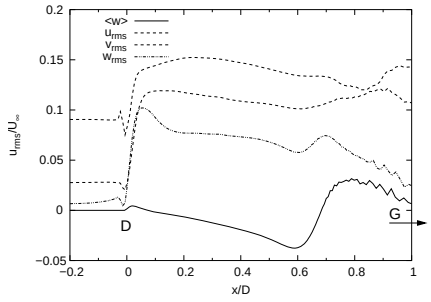

Fig. 10. $< w >$ and Reynolds normal stresses along $\overline{DG}$

under the cusp has still a vertical component pointing outwards of the cavity in the initial region of the shear layer. This might also be the reason for the small overshoot in vertical Reynolds normal stresses just after the cusp (figure 10). Else there is no unexpected behaviour in Reynolds stresses within the shear layer until the stagnation region at the cavity's impingement edge is reached.

The *mean stagnation point* at the impingement edge of the cavity is identified by flow reversal in both the u and the w component (figure 11(a) and 11(b)), by a small region of vanishing kinetic energy of the mean flow field (figure 11(c)) and of a high pressure region 12(a)). This is the region where the circular vortex structure inside the cavity is highly distorted – due to the rounded shoulder of the impingement edge. The stagnation point is somewhat above the left-most part of the shoulder, which leads to backflow at the shoulder. The high pressure at the stagnation point drives high energy flow around the shoulder into the cavity with a velocity magnitude of about one third of the free stream velocity. From the distribution of the kinetic energy of the mean velocity field (figure 11(c)), it could be argued that this effect is more important for driving the vortex inside the cavity than the momentum transport through the shear layer between outer and cavity flow. This statement is supported by the observation that there is a *nearly stagnant region* at $[x/D, z/D] \approx [0.45, -0.1]$ that interrupts the relatively energetic circular motion in the outer part of the cavity. This region is of low mean vorticity and of relatively high pressure (figure 12), which seems to stem from the stagnation point and counteract the circular motion inside the cavity by establishing an adverse pressure region for the fluid coming upstream from and being accelerated by the shear layer.

Turbulence is mainly high (and being generated) in the shear layer and around the stagnation point (figure 12(c)). After having been convected into the cavity around the shoulder of the impingement edge, it quickly looses intensity. Around the stagnation point, there are surprisingly high values of spanwise Reynolds stresses. Such high values have already been observed in other reattaching flows near the mean stagnation point (as e.g. Castro and Haque [12] or Manhart and Wengle [13]). The *vortex core* is characterised as a region of generally low turbulence intensity and constant vorticity, distributed in a circular shape.

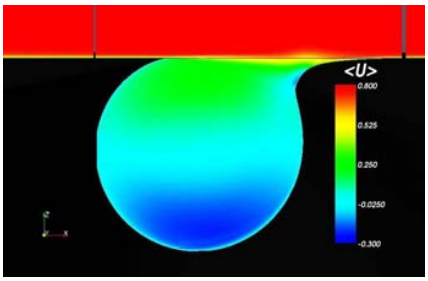

(a)

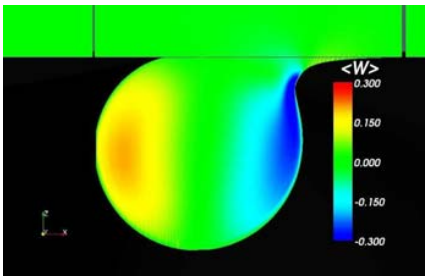

(b)

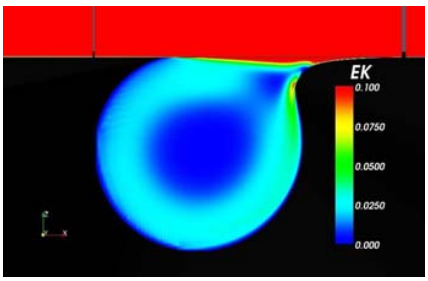

(c)

Fig. 11. Time-averaged contour plot of (a) pressure, (b) wall-normal velocity and (c) Kinetic energy

V. Conclusion

The *shear layer* above the cavity is a highly active region that is excited by both, the turbulent boundary layer coming from upstream and the fluctuations coming from inside the cavity. The fluctuations reach approximately standard values

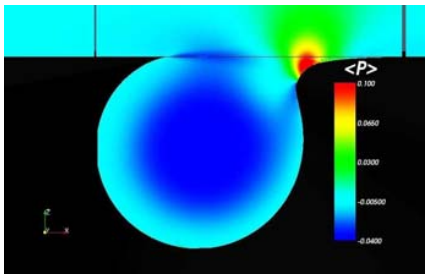

(a)

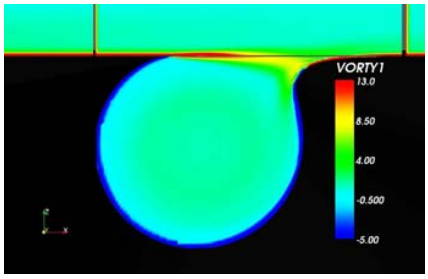

(b)

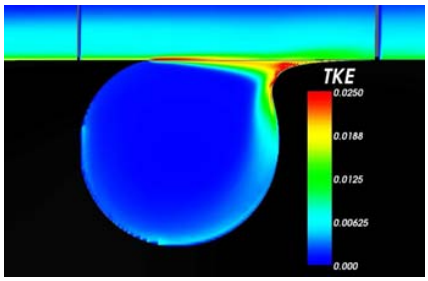

(c)

Fig. 12. Time-averaged contour plot of (a) pressure, (b) spanwise vorticity and (c) Turbulence kinetic energy

of a mixing layer after a strong amplification immediately after separation from the cusp of the cavity. The low pressure in the shear layer entrains fluid from inside the cavity and thus contributes to the rotational motion in the cavity. As the flow reaches the zone around the *stagnation point* at the impingement edge of the cavity, it runs into a high pressure region. This seems to interrupt the rotational motion for a small part of the flow field. The high pressure of that zone drives high-energy packets of fluid into the cavity that travel along the wall in the outer part of the cavity. These high-energy packets seem to be responsible for the largest contribution to the rotational motion in the *vortex core*. This is located in the central part of the cavity and consists of solid body rotation without much turbulence activity. The boundary layer that forms between the main vortex and the cavity wall is far from behaving like a canonical zero pressure gradient boundary layer along a flat plate. This seems to be the result of the high energy packets that transport turbulence and vorticity along the outer part of that boundary layer and due to curvature effects. Turbulence modelling for this part of the cavity flow might not be successful if the complicated structure of the driving mechanism was not taken into account.

In the next step, a proper orthogonal decomposition will be performed to extract high energy modes. The the reduced-order model can be try out for this setting of the cavity flow.

ACKNOWLEDGMENT

The authors would like to thank Dr.Rafaele Donelli and Dr.Pierluigi Iannelli for fruitful collaborations. The support from European Commission of Vortexcell2050 under a contract number AST4-CT-2005-012139 is gratefully acknowledged.

REFERENCES

[1] J. Smagorinsky. General Circulation experiments with the primitive equations. *Mon. Wea. Rev.* , 91:99-164 , 1963.
[2] M. Germano, U. Piomelli, P. Moin and W. H. Cabot. A Dynamic Subgrid-Scale Eddy Viscosity Model. *Physics of Fluids A*, 3(7):1760-1765 ,1991.
[3] C. Meneveau, T. S. Lund and W. H. Cabot. A Lagrangian dynamic subgrid-scale model of turbulence. *Journal of Fluid Mechanics*., 319:353-385, 1996.
[4] N. Peller, A. Le Duc, F. Tremblay, and M. Manhart. High-order stable interpolations for immersed boundary methods. *International Journal for Numerical Methods in Fluids*, in press, 2006.
[5] M. Manhart. A zonal grid algorithm for DNS of turbulent boundary layers. *Computers & FLuids*, 33(3):435–461, 2004.
[6] J.H.Ferziger and M. Peric. *Computational Methods for Fluid Dynamics*. Springer, 1996.
[7] P. R. Spalart. Direct simulation of a turbulent boundary layer up to $R_\theta = 1410$. *Journal of Fluid Mechanics*., 187:61-98, 1988.
[8] M. Manhart and R. Friedrich. DNS of a turbulent boundary layer with separation. Int. J. Heat and Fluid Flow, 23(5):572-581, 2002.
[9] T. S. Lund, X. Wu and K. D. Squires. Generation of Turbulent Inflow Data for Spatially-Developing Boundary Layer Simulations. *Journal of Computational Physics*, 140:223-258, 1998.
[10] F. Tremblay, M. Manhart, and R. Friedrich. DNS and LES of flow around a circular cylinder at a subcritical Reynolds number with Cartesian grids. In R. Friedrich and W. Rodi, editors, *LES of complex transitional and turbulent flows*, p.133-150, Dordrecht, 2001. Kluwer Academic Publishers.
[11] H.H. Fernholz ,P.J. Finley. The incompressible zero-pressure-gradient turbulent boundary layer: an assessment of the data. *Prog Aerospace Sci*, 32:245-311
[12] I.P. Castro and A. Haque. The structure of a turbulent shear layer bounding a separation region. *J. Fluid Mech.*, 179:439–468, 1987.
[13] M. Manhart. Vortex shedding from a hemisphere in a turbulent boundary layer. *Theoretical and Computational Fluid Dynamics*, 12(1):1–28, 1998.